INSTITUTE OF PHYSICS PUBLISHING NONLINEARITY

Nonlinearity **15** (2002) 1699–1715 PII: S0951-7715(02)30010-0

Dynamics of the convergence towards a self-similar blowup solution in a simplified model of aggregation

Cristián Huepe[1]

James Franck Institute, University of Chicago, 5640 S. Ellis Avenue, Chicago, IL 60637, USA

E-mail: cristian@control.uchicago.edu

Received 17 October 2001, in final form 26 June 2002
Published 19 August 2002
Online at stacks.iop.org/Non/15/1699

Recommended by F Otto

Abstract

The dynamics of the finite-time blowup solutions of a parabolic–elliptic system of partial differential equations is studied. These equations arise when modelling chemotactic aggregation or a dissipative gravitational collapse. Radial self-similar blowup solutions on a bounded domain are analysed by perturbing the known analytic solutions of the corresponding unbounded problem. The dynamics followed by general initial conditions leading to these blowup solutions is studied numerically. They are shown to converge to the self-similar profile in a non-uniform way. In similarity coordinates (where self-similar blowup solutions appear as stationary), their convergence properties are characterized by the eigensystem associated to the linearized time evolution equations. The resulting eigenvalues λ_n and eigenvectors are presented for various values of the space dimension parameter d. The asymptotic behaviours of λ_n are found for $d \to 2$ and for large d. A simple numerical formulation for this problem, obtained by reparametrizing the blowup profile dynamics, is presented in the appendix. It simplifies the numerical task by reducing the number of resolution points needed to describe the blowup profile when approaching the singularity.

Mathematics Subject Classification: 35B35, 35J55, 35J60, 47H06, 65F15

1. Introduction

Finite-time blowup dynamics appear in several physical realizations. The pinch-off when a fluid breaks up into two separate bodies [1–3], the gravitational collapse of a star into a

[1] New address: ESAM, Technological Institute, Northweston University, 2145 Sheridan Road, Evanstan, IL 60208-3125, USA. E-mail: cristian@cookiemonster.esam.nwu.edu

0951-7715/02/051699+17$30.00

black hole [4, 5] and the blowup solutions in the nonlinear Schrödinger equation [6, 7], among others [8–11], are all examples of the same class of problem [12]. In these systems, smaller and smaller scales are produced in a finite time. When a certain critical blowup time T_c (in which the equations develop singularities) is approached, the lack of typical external scales leads naturally to a self-similar behaviour.

The numerical study of blowup solutions presents several difficulties. As the system approaches the singularity, smaller scales need to be resolved in space and time. Although the balance of the governing terms in the equations of motion often gives us the scaling laws near T_c, it is, in general, not known how to use this analytical information to produce efficient numerical algorithms.

In this paper, we study a parabolic–elliptic system of partial differential equations for which the analytic blowup solutions on an unbounded domain are known [13]. We explore the self-similar blowup solutions for other boundary conditions and perform a linearized perturbation analysis to understand how generic blowup solutions converge to a self-similar profile. We also present a simple numerical technique that helps us resolve the small spatial scales that appear when the system approaches T_c. By studying in detail this relatively simple mathematical system, we expect to understand some general properties of the blowup dynamics and to gain insight that will help us develop more efficient numerical tools for this class of problems.

The paper is organized as follows. In section 2 we present the equations and introduce the changes of variables that take them to our working forms. Section 3 studies the self-similar blowup solutions on bounded domains, and relates them to perturbations over the known analytic solutions on unbounded domains. The dynamics towards the self-similar blowup profile is shown in section 4. In section 5 we study the stability and convergence properties of the blowup profile as a function of the dimension d. Finally, section 6 concludes. The appendix describes the numerical techniques we used to integrate the equations in time.

2. Definition of the system

Consider the parabolic–elliptic system of equations for $\rho(\vec{x}, t)$ and $c(\vec{x}, t)$:

$$\begin{aligned} &\partial_t \rho = \Delta\rho - \nabla \cdot (\rho \nabla c) \\ &-\Delta c = \rho, \end{aligned} \tag{1}$$

where ∇ and Δ are defined in a d-dimensional space. This system is a simplification of the Keller–Segel model for chemotactic aggregation, with ρ and c the bacteria and chemo-attractant densities, respectively [14]. It can also be interpreted as describing the dissipative dynamics of a mass density ρ interacting with itself through the gravitational potential c [15].

In this paper, we will concentrate on the study of radial solutions for ρ and c that blow up at the origin[2]. Our analysis will be restricted to $d \geqslant 2$, which is a necessary condition for (1) to produce finite-time singularities [16]. In this framework, it is useful to define

$$h(r, t) = \frac{1}{2r^{d-2}} \int_0^r \rho(r, t) r^{d-1} \, \mathrm{d}r. \tag{2}$$

Expressing (1) in terms of $h(r, t)$ we obtain

$$\partial_t h = \partial_r^2 h + \left(\frac{d - 3 + 2h}{r} \right) \partial_r h + \frac{2(d-2)h}{r^2} (h - 1). \tag{3}$$

When blowup occurs, ρ diverges at the origin as t approaches T_c while the width of the blowup region shrinks to zero (see figure 1). In the $h(r, t)$ representation, this appears as the collapse towards the origin of a self-similar (scale-invariant) profile (see figure 4).

[2] The solutions of (1) may follow various dynamical behaviours which are thoroughly studied in [13].

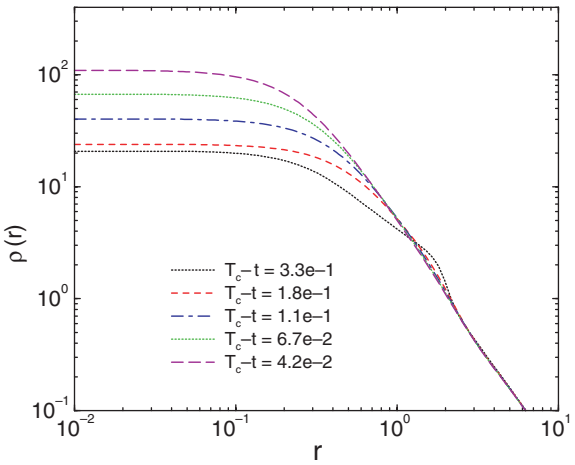

Figure 1. Density ρ versus radius r for various values of time t, with $d = 3$. The profiles correspond to a numerical integration of (1) that will blow up at $t = T_c$. As t approaches T_c, $\rho(r)$ tends to a self-similar profile that will diverge at the origin.

Equation (3) is invariant with respect to the transformation $r' = r/L$ and $t' = t/L^2$. Motivated by this scale invariance, we define the *similarity variables*

$$\eta = \frac{r}{\sqrt{T_c - t}}, \tag{4}$$

$$\tau = -\log(T_c - t). \tag{5}$$

Writing $H(\eta, \tau) = h(r, t)$ in terms of the new variables, equation (3) becomes

$$\partial_\tau H = \partial_\eta^2 H + \left(\frac{d - 3 + 2H}{\eta}\right)\partial_\eta H + \frac{2(d-2)H}{\eta^2}(H - 1) - \frac{\eta}{2}\partial_\eta H. \tag{6}$$

In this formulation, self-similar blowup profiles satisfy $\partial_\tau H(\eta, \tau) = 0$. They can therefore be found as the τ-independent solutions of (6).

3. Self-similar blowup solutions

In this section, we study the self-similar blowup profiles for both bounded and unbounded domains of η. While only the latter have known analytical expressions [13], we will show that by perturbing them we can match most boundary conditions in the bounded domain case. The linear analysis around the analytical solutions (presented in section 5) is therefore relevant for both cases.

As shown in the previous section, a self-similar blowup profile $H_s(\eta)$ satisfies

$$\partial_\eta^2 H_s + \left(\frac{d - 3 + 2H_s}{\eta}\right)\partial_\eta H_s + \frac{2(d-2)H_s}{\eta^2}(H_s - 1) - \frac{\eta}{2}\partial_\eta H_s = 0. \tag{7}$$

The boundary condition for H_s at $\eta = 0$ is obtained by imposing the condition that $\rho(r, t)$ does not diverge for $r \to 0$. Indeed, using the definition of $h(r, t)$ (2), we have that

$$\rho(r, t) = \frac{2(d-2)h(r, t)}{r^2} + \frac{2\partial_r h(r, t)}{r}. \tag{8}$$

Therefore, to obtain a non-diverging density ρ at all times, $h(r, t)$ must vanish at least as r^2 for $r \to 0$ or, equivalently, H_s/η^2 must remain bounded as $\eta \to 0$. In order to have $\rho(\eta) \geqslant 0$, we must also satisfy $H_s \geqslant 0$ and $\partial_\eta(\eta^{d-2} H_s) \geqslant 0$ for all η in the domain of the problem.

One more boundary condition is needed to specify completely a solution for H_s. The possible resulting scenarios are studied in the following paragraphs.

3.1. Unbounded domain analytic solutions

Let us first consider the case of an unbounded domain in η where the supplementary boundary condition is imposed through the asymptotic behaviour $\eta\partial_\eta H_s(\eta) \to 0$ for $\eta \to \infty$. For this case, it has been rigorously proven in [13] that there is a countable number of solutions to equation (7). Each solution can be labelled by a non-negative integer N, where $H_N(\eta)$ intersects the line $H = 1$ precisely $N + 1$ times. One of the main properties of this system is that H_0 has an analytic expression [13],

$$H_0(\eta) = \frac{2\eta^2}{2(d-2)+\eta^2}. \tag{9}$$

It was shown in [13] that $H_0(\eta)$ is the most stable of the $H_N(\eta)$, with only one unstable mode which amounts to changes in T_c. In spite of the presence of this mode, the dynamics of $h(r, t)$ will make $H(\eta, \tau)$ converge to $H_0(\eta)$, as opposed to what would happen in a standard convergence to a stationary solution. This is a generic behaviour in finite-time blowup systems. It will be discussed in more detail in section 5.

3.2. Bounded domain solutions

Consider the blowup dynamics of $h(r, t)$ with a given boundary condition at a fixed $r = r^*$. In similarity variables, this corresponds to fixing $H = H^*$ at a moving $\eta^*(t) = r^*/\sqrt{T_c - t}$. For $t \to T_c$, the position η^* of this boundary condition will be displaced towards infinity. For realistic boundary conditions imposed at a finite value of $r = r^*$, we are therefore also interested in solutions which are stationary in similarity variables and which will not diverge for $\eta \to \infty$. This analysis provides a selection criterion that guarantees that the stable profile H_0 on an unbounded domain (the only one studied throughout the rest of the paper) is also relevant for the analysis of the more physical case with a boundary condition at a fixed $r = r^*$.

To explore the boundary conditions for $\eta \to \infty$, let us first study the solutions of (7) by imposing initial conditions at $\eta = 0$, rather than the original boundary conditions at $\eta = 0$ and $\eta = \eta^*$. An analogy can then be drawn between equation (7) and a dynamical initial value problem in which η would correspond to the time variable. In this context, we will refer to 'perturbations' and 'divergent solutions' with respect to variations in η. It must be stressed, however, that we are studying the stationary solutions H_s of (7), and not considering the dynamics in time of the system.

Figure 2 shows several numerical solutions of equation (7) for $d = 3$. The boundary conditions were fixed only at $\eta = 0$. As explained above, in the analytic problem this boundary condition is that $\rho(r, t)$ does not diverge for $r \to 0$. This fixes $H_s(0) = \partial_\eta H_s(0) = 0$ for all the shooting solutions. The numerical shooting problem must therefore be integrated by imposing the value of the second derivative $\partial_\eta^2 H_s(0) = 2 + \Delta$. The different solutions are then scanned by changing the value of Δ. Note that for $\Delta = 0$ we have $H_s = H_0$ and that for $\Delta = 560$, H_s is close to H_1. The data in figure 2 suggest that, for a large enough η, any perturbation over a H_N solution diverges exponentially in η.

In order to explore this idea, we study how the distance between two nearby solutions changes as η grows. Let us define

$$\vec{Q} = (H_s, \partial_\eta H_s), \tag{10}$$

$$\vec{P} = \partial_\eta \vec{Q}. \tag{11}$$

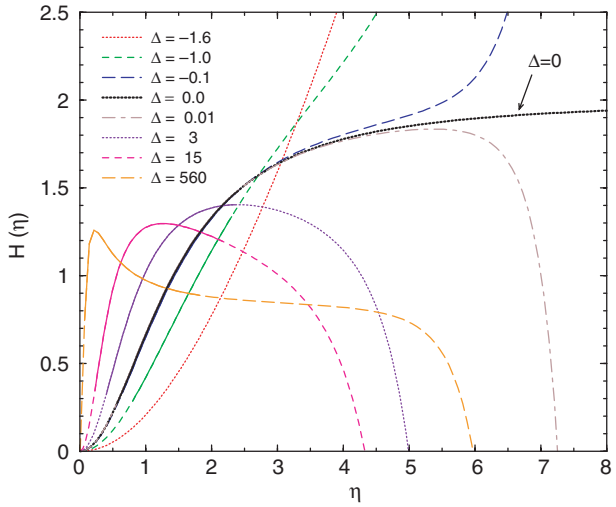

Figure 2. Numerical shooting solutions $H_s(\eta)$ of equation (7) with $d = 3$ and the boundary conditions $H_s(0) = 0$ and $\partial_\eta^2 H_s(0) = 2 + \Delta$. Solid lines indicate segments with $\mathrm{Re}(\lambda_+) < 0$, in which nearby solutions will remain close as η grows. Broken lines are segments with $\mathrm{Re}(\lambda_+) > 0$, where nearby solutions will diverge from each other as η grows (see text). The line in bold is the analytical solution H_0, for which $\Delta = 0$.

Any self-similar blowup profile $H_s(\eta)$ can be viewed as a 'trajectory' (parametrized by η) in the 'phase plane' defined by $\vec{Q}$. The distance $\vec{q}$ between two nearby trajectories in this space follows the equation

$$\partial_\eta q_i = \frac{\partial P_i}{\partial Q_j} q_j, \tag{12}$$

where P_i, Q_j and q_i indicate the components of $\vec{P}$, $\vec{Q}$ and $\vec{q}$, respectively. This means that the eigenvalues λ_i of the Jacobian matrix of the phase plane representation of (7) $M_{ij} \equiv \partial P_i / \partial Q_j$ will determine the behaviour of the distance between two nearby H_s solutions as η grows. If the real parts of all the λ_i are negative, the q_i decrease and nearby solutions of (7) will converge as η grows. In contrast, if there is a positive $\mathrm{Re}(\lambda_i)$, the q_i increase and solutions will diverge as η grows. Using (7), the two eigenvalues (λ_+ and λ_-) of M_{ij} are found to be

$$\lambda_\pm = A \pm \sqrt{B}, \tag{13}$$

where

$$\begin{aligned} A &= \frac{\eta}{4} - \frac{d - 3 + 2H_s}{2\eta} \\ B &= \frac{(d-2)(2 - 4H_s) - 2\eta\partial_\eta H_s}{\eta^2} + \left[\frac{\eta^2 - 2(d-3) - 4H_s}{4\eta}\right]^2. \end{aligned} \tag{14}$$

We have computed λ_+ and λ_- for the H_s solutions in figure 2. The segments with $\mathrm{Re}(\lambda_+) < 0$ are traced with a continuous line while the ones with $\mathrm{Re}(\lambda_+) > 0$, with a discontinuous line. It is apparent that only small segments of the curves have $\mathrm{Re}(\lambda_+) < 0$. Indeed, since $\mathrm{Re}(\lambda_+)$ can only be negative for $A < 0$, for a large enough η and an order one H_s, we must have $\mathrm{Re}(\lambda_+) > 0$. In particular, considering only H_N solutions (which converge to a constant as $\eta \to \infty$), for large η we have $\mathrm{Re}(\lambda_+) > 0$ with $\lambda_+ \sim \eta/2$, which implies that close-by trajectories will diverge as $\sim \exp(\eta^2/4)$. Although this argument is only local (i.e. for solutions close to H_N), numerical evidence and the fact that $\mathrm{Re}(\lambda_+)$ is positive for

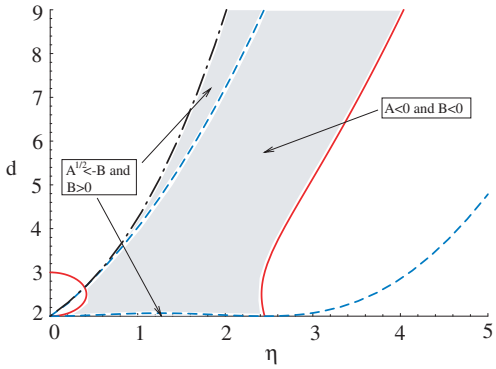

Figure 3. Plot indicating in grey the regions with $\lambda_+ < 0$. The arrows show the zones that satisfy the conditions over A and B for which $\lambda_+ < 0$—see equation (14). Frontier lines are given by $A = 0$ (——), $B = 0$ (- - - -) and $A = \sqrt{-B}$ (— · —).

$\eta^2 > 4H_s + 2d - 6$, suggests that any perturbation over a H_N solution diverges exponentially for η large enough.

Finally, figure 3 shows how λ_+ depends on d for perturbations around the H_0 solution. In the filled region we have $\mathrm{Re}(\lambda_+) < 0$, which corresponds to the union of the zones where either $A < 0$ and $B < 0$, or $A < -\sqrt{B}$ and $B > 0$. The plot is made by using (9) and (14) to find A and B as functions of d and η, and then tracing the frontier curves: $A = 0$ (solid line), $B = 0$ (dashed line) and $A < -\sqrt{B}$ (dot-dashed line). We observe that for all d there is a small range in η for which $\mathrm{Re}(\lambda_+) < 0$. Inside this zone, nearby stationary profiles remain close to each other as we vary η.

4. Blowup dynamics

In this section we present the results obtained by integrating directly equation (3), using the numerical techniques described in the appendix. The goal is to study how the $h(r, t)$ profiles converge to a self-similar solution, while following blowup dynamics as $t \to T_c$.

The graph at the top in figure 4 shows the evolution in time of two different initial conditions for $d = 3$. These are chosen as arbitrary functions that will blow up at a finite time T_c. The boundary condition at the origin (imposing a non-diverging $\rho(r, t)$ as $r \to 0$) corresponds to having $h(0) = 0$ and $\partial_r h(0) = 0$. In practice, we only need to impose $h(0) = 0$ at all times since the numerical integration of (3) guarantees that $\partial_r h(0) = 0$ will be satisfied. At the other extreme of the domain, for a given value of r, a no-flux boundary condition $\partial_r \rho = 0$ would imply

$$-4(d-2)\frac{h}{r^3} + 2(d-3)\frac{h_r}{r^2} + 2\frac{h_{rr}}{r} = 0. \tag{15}$$

However, implementing this involved boundary condition is unnecessary since the evolution towards the singularity is mostly independent of the conditions imposed at large r. Instead, we imposed for convenience that $\partial_r h(10^4) = 0$ at all times. On their way to blowup, the $h(r, t)$ profiles will approach $h_0(r, t)$ given by

$$h_0(r, t) = \frac{2r^2}{r^2 + 2(d-2)(T_c - t)}. \tag{16}$$

This function is equivalent to the $H_0(\eta, \tau)$ function introduced in section 3, but expressed in terms of r and t. In the region $10^{-1} \leqslant r \leqslant 10^0$, the graph at the top shows a zone with

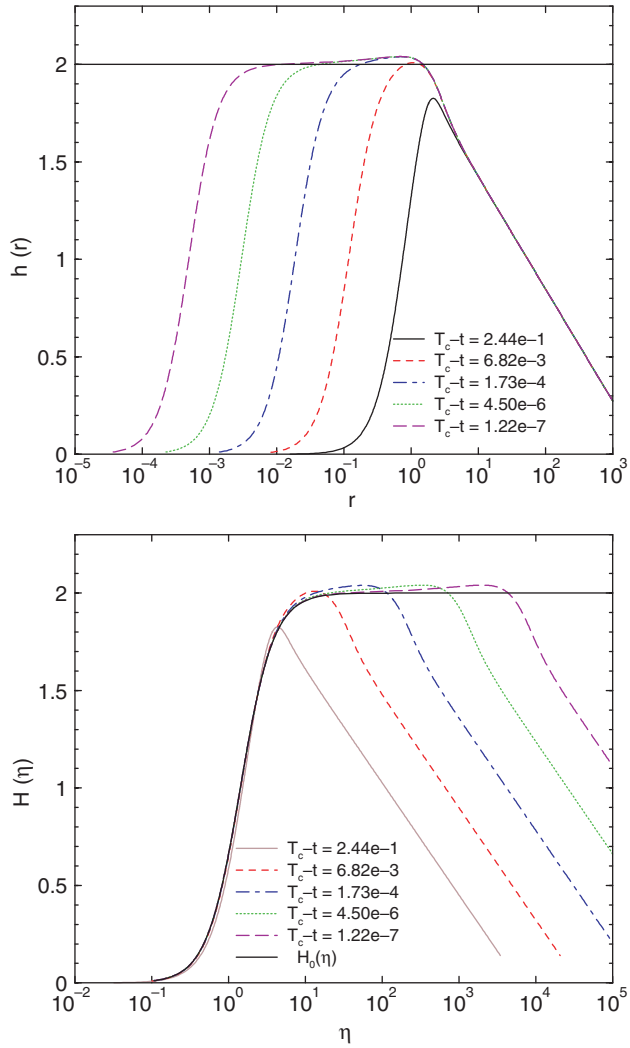

Figure 4. Evolution in time of equation (3) for $d = 3$. Curves are traced at approximately constant slow time intervals $\Delta\tau \approx 3.5$. The graph at the top shows $h(r, t)$ profiles converging to a self-similar blowup solution as they collapse to $r = 0$. For larger values of r, the dynamics evolves too slowly to be seen in the logarithmic timescale τ, and the difference with respect to a self-similar profile h_0 (with limit value for $r \to \infty$ indicated by the line at $h = 2$) appears to be frozen. The graph at the bottom shows the same data in similarity variables $H(\eta, \tau)$ as they evolve to $H_0(\eta)$. The convergence is fast for η small. For η large, the deviations of $H(\eta, \tau)$ with respect to $H_0(\eta, \tau)$ appear to be moving towards larger values of η at an exponential rate in τ.

$h(r, t) < h_0(r, t)$ while the graph at the bottom presents $h(r, t) > h_0(r, t)$. Although they continue to evolve in time, these differences between h and h_0 appear as nearly stationary in the logarithmic (slow) timescale τ of the figures.

We observe in these log–linear graphs that the similarity profile seems to collapse to $r = 0$ at a constant rate in τ. This can be easily understood by solving (16) for the position $r(t)$ of a given point with $h_0 = h_0^*$ fixed. We obtain

$$r^2(t) = \frac{2\,h_0^*(d-2)(T_c - t)}{2 - h_0^*}. \tag{17}$$

Therefore, the collapse rate in logarithmic coordinates is

$$\partial_t \log[r(t)] = \frac{-1}{2(T_c - t)}. \tag{18}$$

In terms of τ, this gives $\partial_\tau \log[r(\tau)] = -\frac{1}{2}$, which explains this approximately constant collapse rate. Note that this result does not depend on the dimension d. Indeed, we have confirmed that equivalent graphs for runs with other values of d show a different similarity profile, but an equivalent collapse rate of the profile towards $r = 0$ (data not shown). This is, however, only an artefact of the logarithmic representation, and simply indicates that the dimension appears within a multiplicative function in the $r(t)$ dynamics. From equation (17) we can verify that the collapse is in fact faster for higher dimensions.

The bottom graph on figure 4, displays the same data as the top one, but now in similarity coordinates. The profile near $\eta = 0$ converges towards the similarity solution which here appears as the stationary curve $H_0(\eta)$. This convergence is non-uniform: small differences $|H(\eta, \tau) - H_0(\eta)|$ are damped faster near $\eta = 0$. Note that for large values of η, these differences do not appear to change in form, but only seem to be displaced to larger values of η at a constant rate in this log–linear representation. The explanation for these observations is given in section 5.

5. Convergence properties of the blowup profile

The blowup solutions converge to a self-similar profile which can be found, in similarity variables, as the τ-independent solutions H_s to equation (6). In this section, we examine the convergence dynamics by solving the eigensystem associated to the time-evolution operator in this equation, linearized around H_s.

Linearizing (6) about a stationary solution H_s we obtain

$$\partial_\tau \Phi(\eta, \tau) = \hat{\Omega}[H_s]\Phi(\eta, \tau), \tag{19}$$

where the linear operator $\hat{\Omega}$ is defined as

$$\hat{\Omega}[H_s] = \frac{\partial^2}{\partial \eta^2} + \left[\frac{d - 3 + 2H_s}{\eta} - \frac{\eta}{2}\right]\frac{\partial}{\partial \eta} + \frac{2\eta \partial_\eta H_s + 2(d-2)(2H_s - 1)}{\eta^2}. \tag{20}$$

Consider the associated eigenvalue problem $\hat{\Omega}\phi(\eta) = \lambda\phi(\eta)$, with the following boundary conditions: $\phi_i(\eta) \to \eta^2$ as $\eta \to 0$ and $\phi_i(\eta)e^{-\eta} \to 0$ for $\eta \to \infty$ [13]. Each eigenfunction ϕ_i (related to the eigenvalue λ_i) corresponds to a small perturbation mode with an amplitude that evolves as $e^{\lambda_i \tau} = (T_c - t)^{-\lambda_i}$.

It has been rigorously proven in [13] that the eigenvalue problem associated to $\hat{\Omega}[H_N]$ (where H_N is any of the countable stationary solutions of (7) described in section 3.1) has $N+1$ unstable modes, one of which corresponds to changing the blowup time T_c. The appearance of anomalous positive eigenvalues, such as this one associated with the arbitrariness in T_c, has been studied quite generally in [2]. It is due to the way that symmetries in the original PDE (3) transform to similarity variables. We can, therefore, focus on perturbations over the stationary solution H_0 defined in (9) which, in spite of this spurious unstable mode, corresponds to the most stable H_N profile and is thus the only one relevant for the dynamics. The following analytical expression for the $\hat{\Omega}[H_0]$ operator is obtained:

$$\hat{\Omega}[H_0] = \frac{\partial^2}{\partial \eta^2} + \left[\frac{4\eta}{2\epsilon + \eta^2} - \frac{\eta}{2} + \frac{\epsilon - 1}{\eta}\right]\frac{\partial}{\partial \eta} + \frac{2\epsilon(3\eta^4 + 4(2+\epsilon)\eta^2 - 4\epsilon^2)}{(2\epsilon\eta + \eta^3)^2}, \tag{21}$$

where $\epsilon = d - 2$. We will study the eigenvalue problem,

$$\hat{\Omega}[H_0]\phi(\eta) = \lambda\phi(\eta). \tag{22}$$

The asymptotic behaviour for $\eta \to \infty$ of the eigenfunctions is known to be $\phi_i(\eta) \sim \eta^{-2\lambda_i}$ [13]. In order to perform a numerical study, we rewrote (22) in terms of the bounded variables $\Gamma(\eta) = \phi(\eta)\mathrm{e}^{-\eta}$ and $\xi = \eta/(1+\eta)$. There is a numerical advantage in making one additional change of variables when studying the solutions for large ϵ. In that case, all the leading order balancing terms are proportional to ϵ/η^2, so the problem becomes smoother by changing variables through $\eta \to \sqrt{\epsilon}\eta$. The results of the analytical and numerical analysis of this eigenvalue problem are given in the following paragraphs.

5.1. Eigenfunctions

The eigenfunctions of (22) are computed by expressing $\hat{\Omega}[H_0]$ in terms of $\Gamma(\xi)$, discretizing the corresponding operator and diagonalizing the resulting matrix [17]. Figure 5 shows the first four eigenfunctions for $d = 2.2$, 3 and 9. The first eigenmode ϕ_0 corresponds to the unstable eigenvalue $\lambda_0 = 1$ reported in [13]. This is the only eigenfunction that has a known analytical expression given by $F_S^0(\eta) = \eta\partial_\eta H_0(\eta)$. The numerical curve $\phi_0(\eta)$ on figure 5 is in excellent agreement with $F_S^0(\eta)$. Indeed, in the interval shown, the L_1 norm of the relative error is smaller than 2×10^{-4}. Here, η_i is the ith discretization point $\delta\eta_i = \eta_i - \eta_{i-1}$, $\Delta\eta_i = \eta_N - \eta_0$ and the sum is over the $N = 623$ points appearing in figure 5.

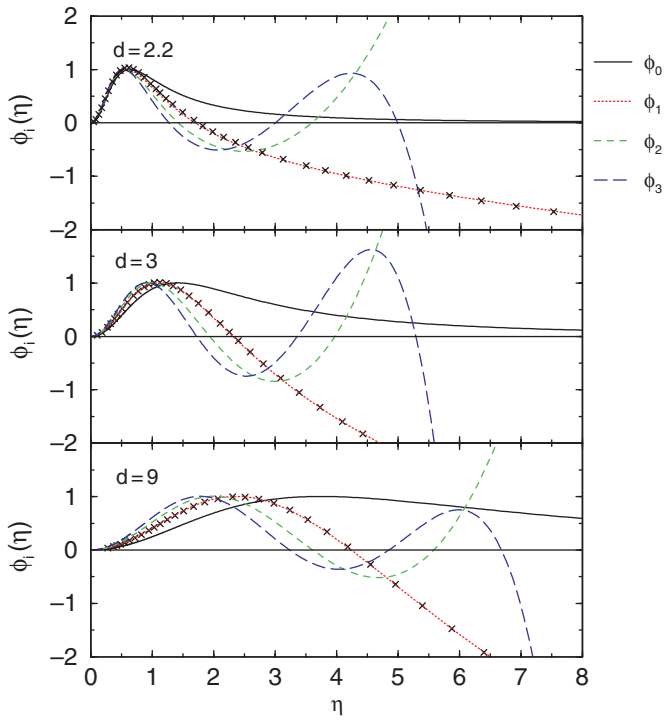

Figure 5. Eigenfunctions (in similarity variables) of the linearized time-evolution operator $\hat{\Omega}[H_0]$ given in (22), for three different values of the dimension parameter d. The eigenfunctions presented correspond to the four largest eigenvalues as indicated. Outside of the displayed region, the asymptotic behaviour for large η is $\phi_\lambda(\eta) \sim \eta^{-2\lambda}$. The crosses show the difference between $H_0(\eta)$ and a numerical solution of (3) for t close to T_c (for $d = 2.2$, $T_c - t = 1.2 \times 10^{-4}$; for $d = 3$, $T_c - t = 1.0 \times 10^{-5}$ and for $d = 9$, $T_c - t = 1.9 \times 10^{-6}$). The agreement with ϕ_1 shows that the linear stability analysis provides an excellent description of the dynamics of the system near the self-similar solution H_0.

The other three eigenfunctions shown in figure 5 are ϕ_1, ϕ_2 and ϕ_3. They correspond to the largest (negative) eigenvalues which have the longest relaxation time and thus govern the dynamics of a perturbation. Beyond the region plotted in figure 5, our numerical results reproduce the analytic asymptotic behaviour $\phi_n(\eta) \sim \eta^{-2\lambda_n}$ (data not shown) [13]. This polynomial divergence in η is a consequence of the change to similarity coordinates. It reflects the fact (pointed out in section 4) that the differences with respect to $H_0(\eta)$ are displaced to larger values of η at an exponential rate in τ. This can be shown as follows. Consider the perturbation $\Delta H(\eta, \tau) = H(\eta, \tau) - H_0(\eta)$, which we decompose into its different modes ΔH_n such that $\Delta H_n(\eta, \tau) = e^{\lambda_n \tau}\phi_n(\eta) \sim e^{\lambda_n \tau}\eta^{-2\lambda_n}$ (for large values of η). The evolution in time of any ΔH_n mode can be viewed as a displacement on the η-axis of each point $\Delta H_n^* \equiv \Delta H_n(\eta^*, \tau)$. The position η^* of ΔH_n^* will be

$$\eta^* = (\Delta H_n^*)^{-1/(2\lambda_n)} e^{\tau/2}, \tag{23}$$

which explains the exponential rate in τ at which perturbations are displaced for large values of η. Note that $\partial_\tau \log[\eta^*(\tau)] = \frac{1}{2}$ does not depend on τ or λ_n. This is again a consequence of the logarithmic time derivative (see section 4). It explains why in the log–linear plots in figure 4 perturbations appear to be moving at a constant rate in τ and without changing their form (since all modes are shifted at the same rate).

5.2. Eigenvalues

The eigenvalues of (22) were computed as functions of d. The numerical value obtained for λ_0 is in excellent agreement with the corresponding exact analytical result $\lambda_0^{\mathrm{A}} = 1$ [13]. For $d = 3$ we obtained $|\lambda_0 - \lambda_0^{\mathrm{A}}| \sim 2 \times 10^{-5}$. Figure 6 shows λ_1, λ_2 and λ_3 for $2 < d < 12$. As d decreases, the λ_n values also decrease until a minimum is reached at $\lambda_n^* = \lambda_n(d^*)$.

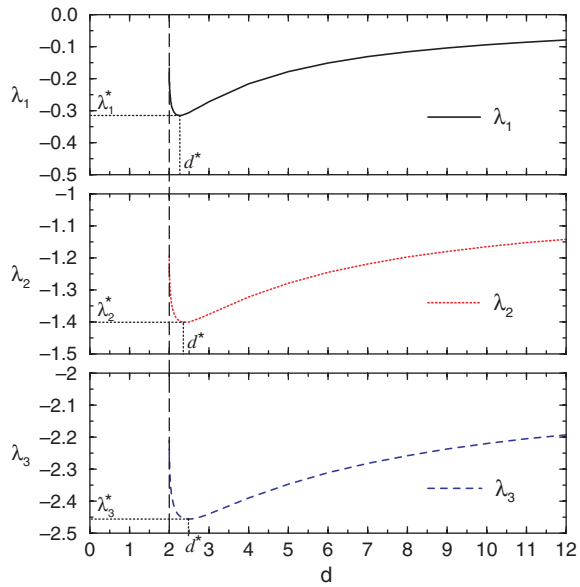

Figure 6. Largest negative eigenvalues of the operator $\hat{\Omega}[H_0]$ defined in (21), as a function of the dimension parameter d. When d decreases, the values of λ_1, λ_2 and λ_3 decrease until the minimal values $\lambda_n^* = \lambda(d^*)$, reported in table 1, are reached. As d approaches the critical dimension 2, the eigenvalues increase rapidly to reach an integral value for $d \to 2$.

This non-trivial behaviour means that for decreasing values of $d > d^*$, while the blowup dynamics becomes slower, the system converges to a self-similar profile following a faster power-law $\sim (T_c - t)^{-\lambda_n}$. The numerical values obtained for d^* and λ_n^* are given in table 1. As d decreases further, for $2 < d < d^*$, the eigenvalues rapidly increase to reach a finite asymptotic value for $d \to 2$.

Let us now study the asymptotic behaviour of the eigenvalues for large d and for $d \to 2$. These limits correspond to the upper and lower bounds within which the self-similar blowup solutions exist, which suggests that they may be treated analytically. Indeed, the similarity solution H_0 can be viewed as being made of an inner region (small η) where $\partial_\eta H_0(\eta)$ becomes large and the density ρ grows steeply, and an outer region (large η) where $\partial_\eta H_0(\eta)$ is typically small and ρ preserves a smooth curvature. Both regions coincide with the ones appearing in figure 5 for $\phi_\lambda(\eta)$, the inner presenting an oscillatory behaviour and the outer, a power-law behaviour. For $d \to \infty$, the inner region follows $H_0(\eta) \sim \eta^2$ and covers all the values of η up to infinity, allowing an analytic solution which can be used to study this asymptotic limit. For $d \to 2$, the inner region collapses to $\eta = 0$ while the outer H_0 converges to the constant profile $H_0(\eta) = 2$. The asymptotic behaviour appears when considering the inner region as a thin boundary layer. In figure 7 we have plotted in a log–log graph $|\lambda_1|$, $|\lambda_2| - 1$ and $|\lambda_3| - 2$ as functions of $\epsilon = d - 2$. It is apparent that in both limits $\epsilon \to 0$ and $\epsilon \to \infty$, all curves appear to follow an asymptotic law with each λ_n reaching the value $\lambda_n = -n + 1$.

Table 1. Minimal value λ_n^* and corresponding dimension d^* of the three eigenvalues shown in figure 6.

	λ_1	λ_2	λ_3
d^*	2.267	2.397	2.484
λ_n^*	−0.315	−1.401	−2.456

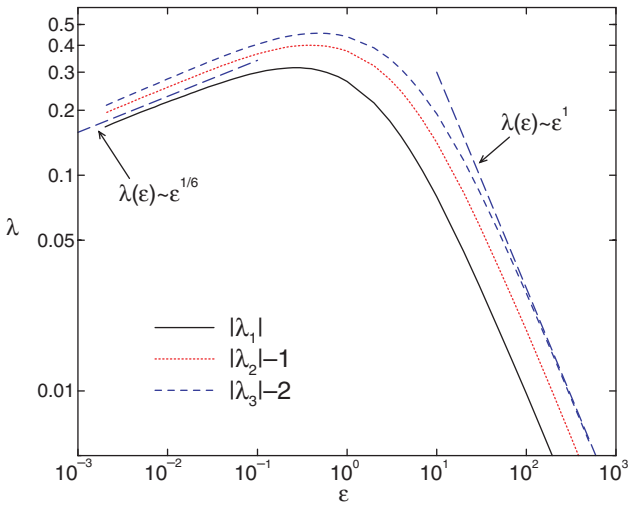

Figure 7. Largest negative eigenvalues of the operator $\hat{\Omega}[H_0]$ defined in (21), as a function of the dimension. The data is the same as in figure 6, but here the eigenvalues λ_n are shifted. We plot $|\lambda_n| - (n-1)$ as a function of $\epsilon = d - 2$ so that the asymptotic values of each curve for $\epsilon \to 0$ and for $\epsilon \to \infty$ are equal to 0. In this log–log representation, the asymptotic scaling laws appear clearly and are properly fitted by the slopes of the dashed lines.

The asymptotic behaviour for large d can be found analytically through a perturbation analysis of the eigenvalue problem (22). In order to obtain an eigenvalue system at order 0 for $\delta \equiv 1/\epsilon \to 0$, we write (22) in terms of $\xi = \eta/\sqrt{\delta}$ [18]. Setting $\Theta(\xi) = \phi(\eta)$ in the new variables, we have

$$(A + \delta \cdot B)\Theta(\xi) = \lambda\Theta(\xi), \tag{24}$$

with

$$A = \frac{(2-\xi^2)}{2\xi}\frac{\partial}{\partial\xi} - \frac{2(2-3\xi^2)}{\xi^2(2+\xi^2)}, \tag{25}$$

$$B = \frac{\partial^2}{\partial\xi^2} - \frac{2-3\xi^2}{\xi(2+\xi^2)}\frac{\partial}{\partial\xi} + \frac{16}{(2+\xi^2)^2}. \tag{26}$$

Then, expanding $\Theta_n(\xi)$ and λ_n in powers of δ,

$$\Theta_n(\xi) = \Theta_n^{(0)}(\xi) + \delta \cdot \Theta_n^{(1)}(\xi) + \cdots, \tag{27}$$

$$\lambda_n = \lambda_n^{(0)} + \delta \cdot \lambda_n^{(1)} + \cdots, \tag{28}$$

we obtain the zeroth-order problem $A\Theta_n^{(0)}(\xi) = \lambda_n^{(0)}\Theta_n^{(0)}(\xi)$. The solutions for $\Theta_n^{(0)}(\xi)$, satisfying the asymptotic boundary conditions $\Theta_n^{(0)}(\eta) \to \eta^2$ as $\eta \to 0$ and $\Theta_n^{(0)}(\eta)\mathrm{e}^{-\eta} \to 0$ as $\eta \to \infty$ are given by

$$\Theta_n^{(0)}(\xi) = \frac{C_0\xi^2(2-\xi^2)^{1-\lambda_n^{(0)}}}{(2+\xi^2)^2}, \tag{29}$$

where C_0 is an integration constant. The associated eigenvalues are obtained by imposing that the $\Theta_n^{(0)}(\xi)$ are real functions with no singularities. This implies that $\lambda_n^{(0)} = -n + 1$, where n takes the values $n = 0, 1, 2, \ldots$.

The first-order terms in equation (24) produce the relation

$$(A - \lambda_n^{(0)})\Theta_n^{(1)}(\xi) = (\lambda_n^{(1)} - B)\Theta_n^{(0)}(\xi). \tag{30}$$

In order to solve this differential equation, we first find the solution $\Theta_n^{\mathrm{H}}(\xi)$ to the homogeneous equation $(A - \lambda_n^{(0)})\Theta_n^{\mathrm{H}}(\xi) = 0$, which is equivalent to the zeroth-order problem. This gives

$$\Theta_n^{\mathrm{H}}(\xi) = \frac{C_1\xi^2(2-\xi^2)^{1-\lambda^{(0)}}}{(2+\xi^2)^2}, \tag{31}$$

with C_1 the new integration constant. Then, we find a particular solution $\Theta_n^{\mathrm{P}}(\xi)$ of (30):

$$\Theta_n^{\mathrm{P}}(\xi) = \frac{-C_0\mathrm{e}^{-1}\xi^2(2-\xi^2)^{1-\lambda_n^{(0)}}}{(2+\xi^2)^2}(\mathcal{K} + \mathcal{L}) \tag{32}$$

with

$$\mathcal{K} = \left(1 - \lambda_n^{(0)} + \lambda_n^{(1)}\right)\log(2-\xi^2), \tag{33}$$

$$\mathcal{L} = \left(1 - \lambda_n^{(0)}\right)\left[\frac{4(\lambda_n^{(0)} + 2 - \xi^2)(1-\xi^2)}{(2-\xi^2)^2} - \log(2+\xi^2)\right]. \tag{34}$$

The solutions of (30) are thus given by $\Theta_n^{(1)}(\xi) = \Theta_n^{\mathrm{H}}(\xi) + \Theta_n^{\mathrm{P}}(\xi)$. To impose again that the eigenfunctions are nonsingular, the $\mathcal{K}$ term must vanish. The corrections to the eigenvalues therefore satisfy $(1 - \lambda_n^{(0)} + \lambda_n^{(1)}) = 0$. This implies that, to first order in $\delta = \epsilon^{-1}$, we have

$$\lambda_n(\delta) = \lambda_n^{(0)} + \delta \cdot (\lambda_n^{(0)} - 1) + \mathrm{O}(\delta^2), \tag{35}$$

Table 2. Amplitudes K_n and exponents p of the asymptotic behaviour for $\epsilon \to 0$ of the eigenvalues λ_n, as obtained from the data in figures 6 and 7.

	λ_1	λ_2	λ_3
K_n	0.449	0.559	0.627
p	0.158	0.169	0.176

with $\lambda_n^{(0)} = -n + 1$, and n spanning all non-negative integer values. This result agrees with the fits to the numerical data in figure 7. Indeed, assuming an arbitrary expansion of the form $\lambda_n^{(0)} + \tilde{\delta} \cdot \tilde{\lambda}_n^{(1)}$, we obtained the following values for $\tilde{\delta}$ and $\tilde{\lambda}_n^{(1)}$. For $n = 1$, $\tilde{\lambda}_1^{(1)} = -0.958$ and $\tilde{\delta} = \epsilon^{-0.9997}$; for $n = 2$, $\tilde{\lambda}_2^{(1)} = -1.972$ and $\tilde{\delta} = \epsilon^{-1.007}$; and for $n = 3$, $\tilde{\lambda}_3^{(1)} = -2.957$ and $\tilde{\delta} = \epsilon^{-1.002}$.

As we can observe in figure 7, the asymptotic behaviour for $\epsilon \to 0$ appears to be given by $\lambda_n = (-n + 1) + K_n \epsilon^p$. Table 2 presents the numerical values obtained for K_n and p by fitting the small ϵ region of the $\lambda(\epsilon)$ curves in figure 7. In spite of the loss of precision that occurs when evaluating the eigenvalues near $\epsilon = 0$, these results suggest an asymptotic power-law compatible with $p = \frac{1}{6}$ (see figure 7). However, the problem of finding an analytic series in ϵ that describes the behaviour of λ_n in this limit turns out to be non-trivial. Indeed, as $\epsilon \to 0$, the eigenfunctions $\phi_n(\eta)$ develop a boundary layer around $\eta = 0$. We must, therefore, perform a matched asymptotic expansion together with the eigensystem perturbation series. A preliminary analysis indicates that a polynomial stretching of the boundary layer and a polynomial perturbation series do not allow a smooth match between the inner and the outer solutions [18]. This suggests that more involved techniques need to be considered such as multiple boundary layers or an expansion with logarithmic coefficients in ϵ. The complete solution to this problem goes beyond the scope of this paper and will be left for future work.

5.3. Convergence dynamics towards the blowup solution

We will now verify that the linear analysis presented above adequately describes the nonlinear dynamics of the solutions $h(r, t)$ to equation (3) when close to blowup. In order to do this, we first integrate numerically equation (3), expressing the result in similarity variables to obtain $H_{\text{run}}(\eta, \tau)$, and then compute $\Delta H(\eta, \tau) = H_{\text{run}}(\eta, \tau) - H_0(\eta)$ for t close to T_c, where $H_0(\eta)$ is the analytic self-similar solution given in (9). The crosses on figure 5 show the resulting $\Delta H(\eta, \tau)$ for $d = 2.2$ ($T_c - t = 1.2 \times 10^{-4}$), $d = 3$ ($T_c - t = 1.0 \times 10^{-5}$) and $d = 9$ ($T_c - t = 1.9 \times 10^{-6}$). After adequate normalization, each $\Delta H(\eta, \tau)$ curve fits to its corresponding eigenfunction ϕ_1 perfectly. This excellent agreement confirms that the nonlinear dynamics close to blowup is indeed controlled by the least stable eigenmode ϕ_1. All other modes have been damped down to zero amplitude faster.

The eigenvalue λ_1 associated to ϕ_1 governs the evolution of the amplitude of $\Delta H(\eta, \tau)$, which must decay as $(T_c - t)^{-\lambda_1}$. Table 3 compares the value of λ_1 found from this damping rate of the amplitude of $\Delta H(\eta, \tau)$ with the one obtained by computing the numerical eigenvalues of $\hat{\Omega}[H_0]$ (as it was done to produce figure 6). Both values show a satisfactory agreement. The differences can be attributed to the lack of enough numerical precision in integrating $h(r, t)$ in time as it approaches the singularity, and to the difficulties in computing T_c.

Note that the nonlinear dynamics is not governed by the eigenmode ϕ_0 associated to the anomalous positive eigenvalue λ_0. We, therefore, confirm that this mode appears due to the way that the symmetries in the original PDE transform to similarity variables, and does not reflect the existence of an unstable mode in the original dynamics for $h(r, t)$. However,

Table 3. Comparison between the numerical results for the least stable eigenvalue λ_1 obtained through two different methods for three values of the dimension d. Column λ_1^{Ω} is obtained by diagonalizing $\hat{\Omega}[H_0]$ and column λ_1^{damp} from the damping rate of the amplitude of $\Delta H(\eta, \tau)$.

d	λ_1^{Ω}	λ_1^{damp}
2.2	−0.314	−0.302
3	−0.272	−0.269
9	−0.104	−0.105

the ϕ_0 mode will be present in $\Delta H(\eta, \tau)$ if a shift in the blowup time T_c occurs. This fact may become relevant in the study of the blowup dynamics of experimental systems, where T_c can be modified by any external perturbation.

6. Conclusions

We have studied in detail the dynamical solutions of the parabolic–elliptic system of equations (1) that lead to a finite-time singularity. We analysed the self-similar solutions for bounded and unbounded domains, and showed that all dynamical blowup solutions converge to the analytical $H_0(\eta)$ profile (9) in a non-uniform way.

The convergence properties were studied by finding the eigenvalues and eigenfunctions associated to the linearized time evolution equations of the system. It was shown that, when the system is close enough to the critical time, this eigensystem provides a good description of the dynamics of the convergence towards the self-similar blowup solution. It is interesting to note that a numerical eigenvalue analysis equivalent to the one that was carried out in this paper can be performed in other blowup systems. In cases where the analytical self-similar solution is unknown, the $\hat{\Omega}$ operator can still be built by linearizing about a numerical solution which is stationary in similarity variables. The eigenvalue analysis then provides a stability criterion showing which solution is selected by the dynamics. The associated eigenfunction helps us understand how the non-uniform convergence of $h(r, t)$ towards the self-similar profile occurs.

Throughout our analysis, the dimension d was shown to play an important role in the blowup dynamics, as has been observed in other systems [19]. We have found that, if we increase the value of d (with $d > d^*$ for the d^* given in table 1), the self-similar profile will approach blowup faster but the convergence to the blowup profile will be slower (since the most stable eigenvalue will come closer zero). It would be interesting to know if this kind of behaviour is observed in other blowup systems as a function of the dimension or of any other tunable parameter. We have also shown that the study of a blowup system can be extended to values of the dimension parameter in which some analytical progress can be achieved. This technique may also be of help when applied to more involved systems.

Finally, we have described in the appendix an intuitive numerical technique that allows the study of finite-time blowup without the need of implementing an adaptative mesh algorithm.

In conclusion, the numerical and analytical results obtained in this article show that the detailed analysis of this and other relatively simple blowup systems [8] should help us elucidate their general properties and develop techniques for treating finite-time singularities.

Acknowledgments

We wish to thank Leo P Kadanoff for the various comments and suggestions given throughout this work. We also acknowledge very useful scientific discussions with Maximino Aldana,

Todd Dupont, Shankar Venkataramani and Haim Diamant. This project at the University of Chicago is supported in part by the DOE supported ASCI/Alliances Center for Astrophysical Thermonuclear Flashes and in part by the Materials Research Science Center (MRSEC) under NSF DMR 9808595.

Appendix

We describe here the numerical techniques that were used to integrate $h(r, t)$ in time. The main numerical difficulty when dealing with the blowup solutions is the appearance of smaller and smaller scales close to $r = 0$ as t approaches T_c. However, from figure 4 we observe that this problem occurs mainly due to the diverging slope $\partial_r h(r, t)$ as $t \to T_c$, which forces the use of increasing resolution around $r = 0$ if a standard integration method is applied. Our technique is based on the simple remark that the blowup profile can be easily resolved near $r = 0$, even for t very close to T_c, only if the $h(r, t)$ curve is parametrized otherwise (e.g. by using h as a parameter and describing the profile by the $r(h, t)$ function). We will develop below a numerical algorithm based on this idea.

Let us define the nonlinear operator $F[h]$ as

$$F[h] = \partial_r^2 h + \left(\frac{d - 3 + 2h}{r}\right)\partial_r h + \frac{2(d-2)h}{r^2}(h - 1). \tag{A1}$$

Equation (3) then becomes simply

$$\frac{\partial h}{\partial t} = F[h]. \tag{A2}$$

Using the implicit function theorem [20], this relation leads us to an equation for the evolution of $r(h, t)$:

$$\frac{\partial r}{\partial t} = -\frac{F[h]}{\partial_r h}. \tag{A3}$$

After some algebraic manipulations (A3) can be expressed in terms of only operators applied over r. We obtain

$$\frac{\partial r}{\partial t} = G[r], \tag{A4}$$

$$\frac{\partial h}{\partial t} = -\frac{G[r]}{\partial_h r}, \tag{A5}$$

with

$$G[r] = \frac{\partial_h^2 r}{(\partial_h r)^2} - \frac{d - 3 + 2h}{r} + \frac{2(d-2)h}{r^2}(h - 1)\partial_h r. \tag{A6}$$

Consider now the evolving $h(r, t)$ function as a moving curve on the r–h plane. Expressions (A3) and (A4) for $\partial_t r$, or (A2) and (A5) for $\partial_t h$, will then describe displacements of the curve points on the r-axis or the h-axis directions, respectively. Further, in general, we can find the displacement rate of the discretization points in the direction of any angle θ on the r–h plane.

Let us define the r-axis or h-axis displacements for an infinitesimal time lapse δt as $\delta r = (\partial_t r) \cdot \delta t$ or $\delta h = (\partial_t h) \cdot \delta t$, respectively (see figure A1). The displacement vector for a given θ is then

$$\vec{\Delta R} = (\alpha \cdot \delta r, \beta \cdot \delta h), \tag{A7}$$

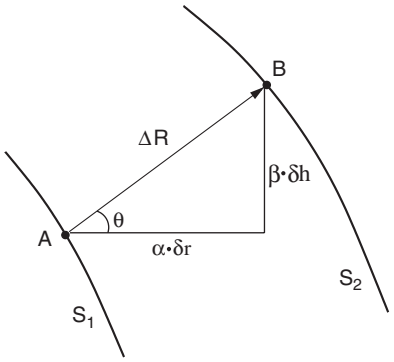

Figure A1. Scheme of the infinitesimal displacement of the discretization point $A = (r_1, h_1)$ on curve $S_1 = h(r, t_1)$ to point $B = (r_2, h_2)$ on curve $S_2 = h(r, t_2)$, due to the evolution from t_1 to t_2 described by equation (3). For a given θ, the distance $|\vec{\Delta R}|$ can be found in terms of $\delta r = (\partial_t r) \cdot \delta t$ and $\delta h = (\partial_t h) \cdot \delta t$ (see text).

with $\alpha + \beta = 1$ and $\tan\theta = (\beta \cdot \delta h)/(\alpha \cdot \delta r)$. By considering an arbitrarily small δt, we thus obtain that the vectorial displacement rate will be $\partial_t \vec{R} \equiv (\partial_t R_r, \partial_t R_h)$, with

$$\frac{\partial R_r}{\partial t} = \frac{F[h]}{\tan\theta - \partial_r h} = \frac{G[r]}{1 - (\partial_h r)\tan\theta}, \tag{A8}$$

$$\frac{\partial R_h}{\partial t} = \frac{F[h]\tan\theta}{\tan\theta - \partial_r h} = \frac{G[r]\tan\theta}{1 - (\partial_h r)\tan\theta}. \tag{A9}$$

For the numerical integrations reported in this paper, we define θ such that $\tan\theta = -1/\partial_r h$. The direction of $\vec{\Delta R}$ is then perpendicular to the curve S_1 (see figure A1). For this choice of θ, we obtain

$$\frac{\partial R_r}{\partial t} = \frac{-F[h]\partial_r h}{1 + (\partial_r h)^2} = \frac{G[r]}{1 + (\partial_h r)^2}, \tag{A10}$$

$$\frac{\partial R_h}{\partial t} = \frac{F[h]}{1 + (\partial_r h)^2} = \frac{-G[r]\partial_h r}{1 + (\partial_h r)^2}. \tag{A11}$$

These relations were used at every time step to compute $\partial_t \vec{R}$. In order not to degrade the numerical precision, the expressions in terms of $F[h]$ were used in regions with large $\partial_h r$, while the ones in terms of $G[r]$ where used where $\partial_r h$ was large. The resulting $\partial_t \vec{R}$ was then introduced into a fourth-order Runge–Kutta method to integrate in time the displacements on the r–h plane of each discretization point [17]. As time evolution progresses, resolution points must be added in the zones where the local curvature of the profile increases. This was done through a standard cubic spline interpolation [17].

References

[1] Eggers J 1997 *Rev. Mod. Phys.* **69** 865–929
[2] Bernoff A J, Bertozzi A L and Witelski T P 1998 *J. Stat. Phys.* **93** 725–76
[3] Zhang W W and Lister J R 1999 *Phys. Fluids* **11** 2454–62
[4] Christodoulou D 1986 *Commun. Math. Phys.* **105** 337
Christodoulou D 1986 *Commun. Math. Phys.* **106** 587
[5] Choptuik M W 1993 *Phys. Rev. Lett.* **70** 9
[6] Fraiman G M 1985 *Sov. Phys.-JETP* **61** 228

[7] McLaughlin D W, Papanicolaou G C, Sulem C and Sulem P L 1986 *Phys. Rev.* A **34** 1200–10
[8] Kammerer C F and Zaag H 2000 *Nonlinearity* **13** 1189–216
Kammerer C F, Merle F and Zaag H 2000 *Math. Ann.* **317** 347–87
[9] Giga Y and Kohn R V 1985 *Commun. Pure Appl. Math.* **38** 297–319
[10] Bricmont J and Kupiainen A 1994 *Nonlinearity* **7** 539–75
[11] Huisken G 1990 *J. Diff. Geom.* **31** 285–99
[12] Barenblatt G I 1979 *Similarity, Self Similarity and Intermediate Asymptotics* (New York: Consultants Bureau)
[13] Brenner M, Constantin P, Kadanoff L P, Schenkel A and Venkataramani S 1999 *Nonlinearity* **12** 1071–98
[14] Keller E F and Segel L A 1992 *J. Theor. Biol.* **119** 355–91
[15] Wolansky G 1970 *Arch. Ration. Mech. Anal.* **26** 399–415
[16] Nagai T 1995 *Adv. Math. Sci. Appl.* **5** 581–601
[17] Press W, Teukolsky S, Vetterling W and Flannery B 1997 *Numerical Recipes in C* (Cambridge: Cambridge University Press)
[18] Hinch E J 1991 *Perturbation Methods* (Cambridge: Cambridge University Press)
[19] Vaynblat D, Lister J R and Witelski T P 2001 *Euro. J. Appl. Math.* **12** 209–32
[20] Friedman A 1971 *Advanced Calculus* (New York: Holt, Rinehart and Winston)